Korean J. Chem. Eng., **31**(2), 350-363 (2014)
DOI: 10.1007/s11814-013-0240-3

pISSN: 0256-1115
eISSN: 1975-7220

Characterization of fluidization regime in circulating fluidized bed reactor with high solid particle concentration using computational fluid dynamics

Benjapon Chalermsinsuwan*,,†, Theeranan Thummakul*, Dimitri Gidaspow***, and Pornpote Piumsomboon*,****

*Fuels Research Center, Department of Chemical Technology, Faculty of Science, Chulalongkorn University, 254 Phayathai Road, Patumwan, Bangkok 10330, Thailand
**Center of Excellence on Petrochemical and Materials Technology, Chulalongkorn University, 254 Phayathai Road, Patumwan, Bangkok 10330, Thailand
***Department of Chemical and Biological Engineering, Armour College of Engineering, Illinois Institute of Technology, 10 W. 33rd Street, Chicago, IL 60616, USA
(*Received 31 August 2013 • accepted 11 November 2013*)

Abstract−The hydrodynamics inside a high solid particle concentration circulating fluidized bed reactor was investigated using computational fluid dynamics simulation. Compared to a low solid particle reactor, all the conventional fluidization regimes were observed. In addition, two unconventional fluidization regimes, circulating-turbulent and dense suspension bypassing regimes, were found with only primary gas injection. The circulating-turbulent fluidization regime showed uniformly dense solid particle distribution in all the system directions, while the dense suspension bypassing fluidization regime exhibited the flow of solid particles at only one side system wall. Then, comprehensive fluidization regime clarification and mapping were evaluated using in-depth system parameters. In the circulating-turbulent fluidization regime, the total granular temperature was low compared to the adjacent fluidization regimes. In the dense suspension bypassing fluidization regime, the highest total granular temperature was obtained. The circulating-turbulent and dense suspension bypassing fluidization regimes are suitable for sorption and transportation applications, respectively.

Keywords: Circulating Fluidized Bed Reactor, Computational Fluid Dynamics Simulation, Fluidization, Total Granular Temperature, Hydrodynamics

INTRODUCTION

The circulating fluidized bed (CFB) is one of the commonly used multiphase flow reactors in the chemical, petrochemical and energy production industries [1,2]. This type of reactor is fundamentally based on the concept of fluidization [3]. The explanation for the obtained situation is because of the balancing between forces acting on the solid particles by input gas or liquid [4,5]. The riser section is the part of a CFB reactor in which the chemical or physical operation normally occurs. Our focus was on the gas-solid particle multiphase flow system. The alteration of solid particle behavior, the fluidization flow regime, mainly depends on the gas inlet velocity [6-9]. The four well-known fluidization flow regimes inside a conventional low solid particle concentration riser are bubbling, turbulent, fast fluidization and pneumatic transport [10-13]. In each fluidization regime, unique specific characteristics are observed. Many researchers have successfully evaluated and explained these various fluidization regimes inside a low solid particle concentration CFB reactor [10,14-16]. In recent years, the CFB reactor has been proposed to be used with high solid particle concentration condition [17-20]. The CFB reactor with low solid particle concentration condition is not suitable for use in some innovative applications due to its low quantity and low contacting chemical reaction area such as carbon dioxide sorption [21] or agricultural product drying [22,23]. Besides, non-uniformity of solid particle concentration distribution was observed inside the low solid particle concentration CFB reactor [7,8]. However, most of the literature research studies mainly discussed the new methodology to operate the reactor in denser mode and their generally observed system hydrodynamics [24-28].

Nowadays, computational fluid dynamics (CFD) simulation is an important tool for designing of many industrial processes. The fundamental theory of the CFD simulation is the solving of mass, momentum and energy conservation equations simultaneously [29]. For multiphase flow systems, two different approaches can be used: Eulerian and Lagrangian. The Eulerian approach is recommended when the quantity of solid particles cannot be occupied by one of gas. Therefore, this approach was selected in this study by separately solving the conservation equations for each phase [30]. Among the various attempts to close the gas-solid particle flow, the kinetic theory of granular flow has found the widest use as a constitutive equation [4,9]. This theory is principally an extension of the kinetic theory of gases [31] to dense gas and solid particle flows with the addition of random movement and non-elastic collision of solid particles in terms of the granular temperature and the restitution coefficients. Due to its many advantages, this mathematical tool is being used for process simulation including CFB reactor [32].

In the literature, some research study about CFD simulation of high solid particle concentration CFB reactor has been reported, but still no concrete fluidization regime clarification and mapping are summarized. After the concept of a high solid particle concentration

†To whom correspondence should be addressed.
E-mail: benjapon.c@chula.ac.th

CFB reactor was first announced by Bi and Zhu [33] and Issangya et al. [34], various CFD simulations with this concept were modeled. They defined the system that operated with solid particle mass flux (G_s) greater than 200 kg/m^2·s and solid particle volume fraction (ε_s) greater than 0.10 as the high solid particle concentration CFB reactor. Cruz et al. [35] developed a new momentum interphase exchange coefficient closure model based on experimental data to predict the solid particle distribution inside high solid particle concentration CFB reactors. CFD simulation of air and fluid catalytic cracking solid particles in the high solid particle concentration CFB reactor was performed by Almuttahar and Taghipour [36]. The challenges in accurate modeling of the solid particle near the wall region were shown. In addition, Almuttahar and Taghipour [17] showed the hydrodynamics of gas-solid particle flow in the same CFB reactor at various fluidization operating conditions. The radial profiles of solid particle velocity in the high solid particle concentration CFB reactor were simulated by Bastos et al. [27] using a three-dimensional CFD simulation. Their model predicted high and low solid particle velocities in the center and wall regions of reactors. Wang et al. [37] developed the hydrodynamic characteristics of the high solid particle concentration CFB reactor, based on the Energy-Minimization Multi-Scale model. The solid particle concentration was dense but still a non-uniform core-annulus flow structure appeared in the bottom reactor section. With the increasing of the reactor height, the solid particle concentration was reduced and the flow structure became more uniform. They claimed that their reactor was operated in dense suspension upflow pattern. In contrast with the above literature, Chalermsinsuwan et al. [21] proposed another high solid particle concentration flow pattern using lower gas inlet velocity from the CFD simulation, called circulating-turbulent fluidization. With this flow pattern, the obtained solid particle concentration was dense and uniform throughout the CFB riser using only primary gas injection. Zhu and Zhu [38], Qi et al. [20,39] and Zhu et al. [40] performed experimental measurement and confirmed the occurrence of the circulating-turbulent fluidization flow pattern inside high solid particle concentration CFB reactor with secondary gas injection.

In this study, the system hydrodynamics inside high solid particle concentration CFB was investigated using commercial CFD simulation, ANSYS FLUENT program. The solid particle flow patterns with various primary gas inlet velocities were illustrated. The validations of system hydrodynamics inside high solid particle concentration CFB reactor were conducted using experimental measurement in Thummakul et al. [41]. Then, comprehensive fluidization regime

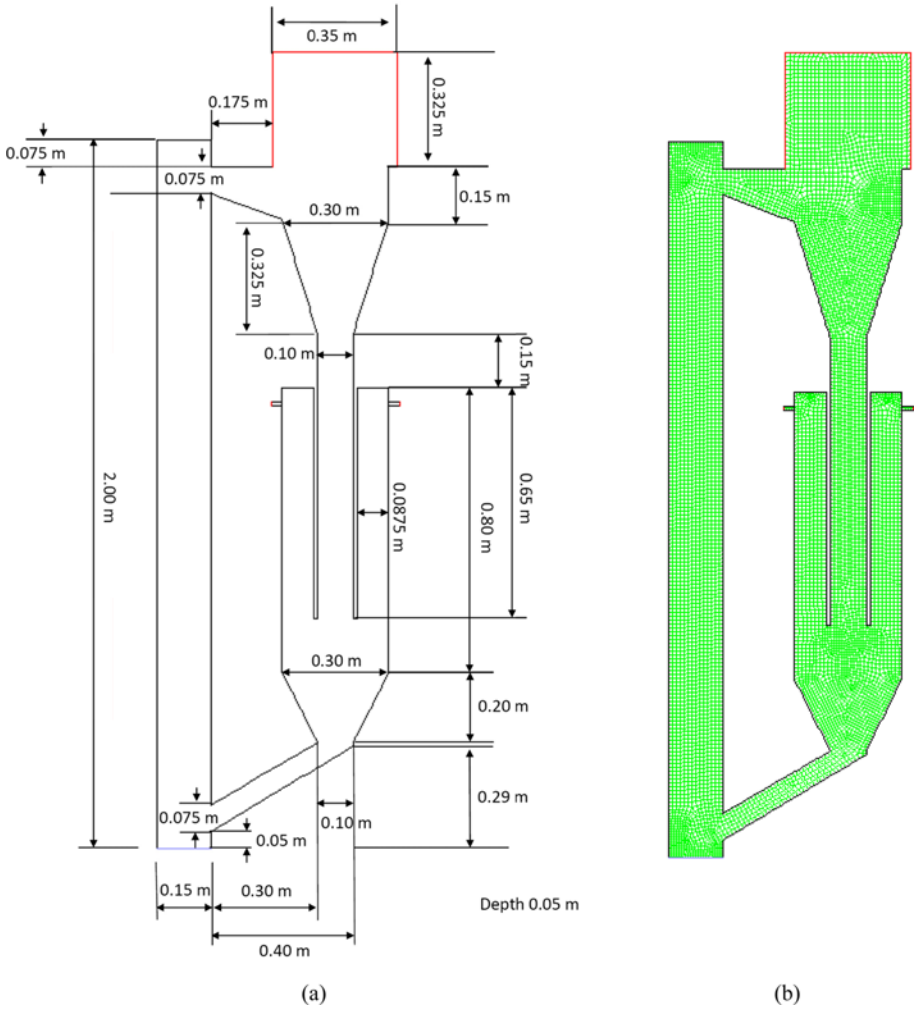

Fig. 1. (a) Schematic drawing of CFB reactor and (b) computational domain of CFB reactor with 8,000 computational cells.

clarification and mapping were summarized using in-depth system parameters such as normal Reynolds stresses and granular temperature. In addition, further fluidization regime explanation and mapping was concluded. This knowledge will enable engineers to efficiently design and operate this reactor.

COMPUTATIONAL FLUID DYNAMICS MODEL

1. System Description and Computational Domain

We performed CFD simulations for an experimental Plexiglas two-dimensional CFB reactor [41]. The cold-flow CFB reactor consisted of three main parts: riser, downer and separating and returning systems. The CFB riser had 2.00 m height, 0.15 m width and 0.05 m depth, while the CFB downer had 1.00 m height, 0.30 m width and 0.05 m depth. For separating and returning systems, the 200 US standard size mesh was used to separate the solid particles from the gas at the top of the reactor and at the small discharge tubes at the CFB downer. The solid particles then fell back to the system and returned to the CFB riser at 0.05 m height from the bottom of the reactor. The ball valve was used to control the solid particle flow from CFB downer to CFB riser. A schematic drawing of the system is shown in Fig. 1(a). At the base of the CFB riser's column, a 200 US standard size mesh was used to support the solid particles. A gas distributor was located directly below the mesh. The gas was conditioned prior to entering the column. First, the gas pressure was controlled to a desired value by a pressure regulator. Then, the gas flowed through a dehydration unit to remove moisture from the gas stream. Finally, the gas inlet velocity was regulated by adjusting the gas stream through a rotameter with a manual valve. The system gas was air with a density (ρ_g) of 1.20 kg/m^3 and a viscosity (μ_g) of 2.00×10^{-5} kg/m·s. The system solid particle was silica sand with a density (ρ_s) of 2,650 kg/m^3 and a mean diameter (d_p) of 380 μm. Initially, 21 kg of solid particles was filled inside the CFB reactor system. The minimum calculated solid particle mass flux inside this system was approximately 300 kg/m^2·s. The other system operating conditions are listed in Table 1.

Table 1. The used system operating conditions and modeling parameters in this study

Description	Value
Width of CFB riser (m)	0.15
Height of CFB riser (m)	2.00
Depth of CFB riser (m)	0.05
Width of CFB downer (m)	0.30
Height of CFB downer (m)	1.00
Depth of CFB downer (m)	0.05
Gas density (kg/m^3)	1.20
Gas viscosity (kg/m·s)	2×10^{-5}
Solid particle density (kg/m^3)	2,650
Solid particle diameter (μm)	380
Gas inlet velocity (m/s)	0.25, 0.75, 1.25, 5.00, 10.00, 25.00
Initial solid particle inside the CFB reactor (kg)	21.00
Outlet system pressure, P (Pa)	101,325
Gravity force, g (m/s^2)	9.81
Solid volume fraction at maximum packing, $\varepsilon_{s,max}$ (-)	0.60
Specularity coefficient, ϕ (-)	0.01
Restitution coefficient between solid particle and wall, e_w (-)	0.90
Restitution coefficient between solid particles, e (-)	0.90

Since a three-dimensional model requires long computation time, we used a two-dimensional computational domain with Cartesian coordinates for the simulation. The computational domain of this study CFB reactor is schematically displayed in Fig. 1(b). The grid independence study was performed as shown in Fig. 2. The procedure for checking the grid independence or effect of computational cell was performed by the incrementing of computational cells. Then, the obtained results for each computational cell were compared. The suitable computational cell is the smallest computational cell that gives the same result as the one with higher computational cell. The employed grids had 4,000, 6,000, 8,000 and 10,000 computa-

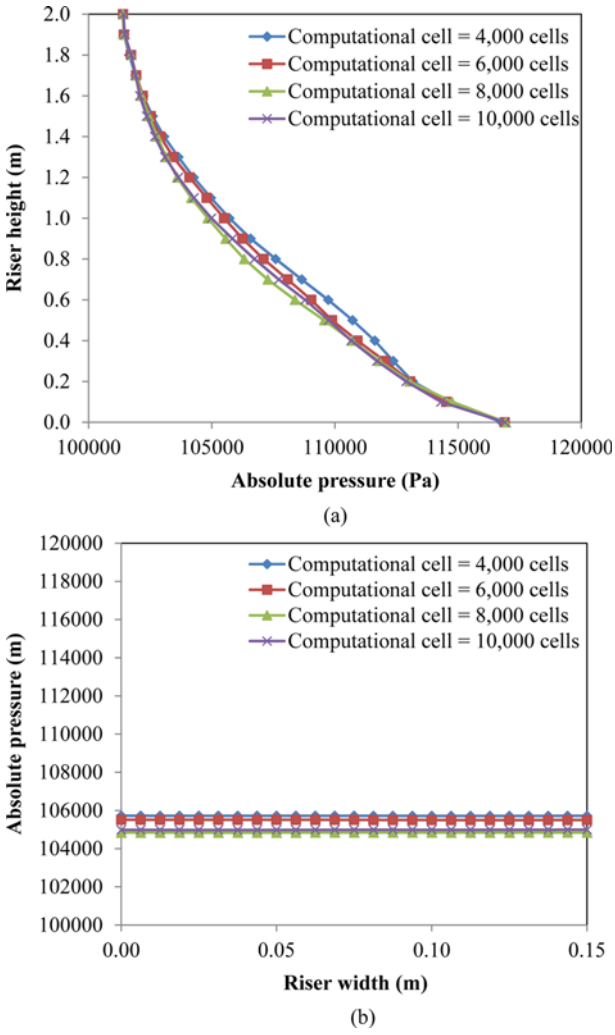

Fig. 2. (a) The axial distributions of time-averaged absolute pressure, and (b) the lateral distributions of time-averaged absolute pressure at 1.00 m CFB riser height with four different computational cells.

tional cells. Fig. 2(a) shows the axial distributions of time-averaged absolute pressure with four different computational cells, while Fig. 2(b) displays the lateral distributions of time-averaged absolute pressure with the same four different computational cells at 1.00 m CFB riser height using 1.25 m/s gas inlet velocity. The selected riser height is the one at half of the riser. From the results, the absolute pressure profiles with 8,000 and 10,000 computational cells were similar. The reason can be explained by the fact that the large computational cells may be too coarse for capturing the real phenomena in the complicated system process in some computational domain area. In the following section, the suitable grid number of 8,000 computational cells then was employed.

2. Mathematical Model

As mentioned, we used the Eulerian approach for simulating the gas-solid particle multiphase flow system using the ANSYS FLUENT program. With the Eulerian approach, the gas and solid parti-

Table 2. A summary of the conservation and constitutive equations used in this study

A. Governing equations;

(a) Conservation of mass;

- Gas phase (g);

$$\frac{\partial}{\partial t}(\varepsilon_g\rho_g)+\nabla\cdot(\varepsilon_g\rho_g v_g)=0 \quad (1)$$

- Solid particle phase (s);

$$\frac{\partial}{\partial t}(\varepsilon_s\rho_s)+\nabla\cdot(\varepsilon_s\rho_s v_s)=0 \quad (2)$$

(b) Conservation of momentum;

- Gas phase (g);

$$\frac{\partial}{\partial t}(\varepsilon_g\rho_g v_g)+\nabla\cdot(\varepsilon_g\rho_g v_g v_g)=-\varepsilon_g\nabla P+\nabla\cdot\tau_g+\varepsilon_g\rho_g g-\beta_{gs}(v_g-v_s) \quad (3)$$

- Solid particle phase (s);

$$\frac{\partial}{\partial t}(\varepsilon_s\rho_s v_s)+\nabla\cdot(\varepsilon_s\rho_s v_s v_s)=-\varepsilon_s\nabla P+\nabla\cdot\tau_s-\nabla P_s+\varepsilon_s\rho_s g+\beta_{gs}(v_g-v_s) \quad (4)$$

(c) Conservation of solid particle fluctuating energy (θ);

$$\frac{3}{2}\left[\frac{\partial}{\partial t}(\varepsilon_s\rho_s\theta)+\nabla\cdot(\varepsilon_s\rho_s\theta v_s)\right]=(-\nabla P_s\bar{\bar{I}}+\tau_s):\nabla v_s+\nabla\cdot(\kappa_s\nabla\theta)-\gamma_s+\varphi_{gs} \quad (5)$$

where v is velocity, ε is volume fraction and I is unit tensor.

B. Constitutive equations;

(a) Gas phase stress (τ_g);

$$\tau_g=\varepsilon_g\mu_g[\nabla v_g+(\nabla v_g)^T]-\frac{2}{3}\varepsilon_g\mu_g(\nabla\cdot v_g)I \quad (6)$$

(b) Solid particle phase stress (τ_s);

$$\tau_s=\varepsilon_s\mu_s[\nabla v_s+(\nabla v_s)^T]-\varepsilon_s\left(\xi_s-\frac{2}{3}\mu_g\right)\nabla\cdot v_g I \quad (7)$$

(c) Collisional dissipation of solid particle fluctuating energy (γ_s);

$$\gamma_s=3(1-e^2)\varepsilon_s^2\rho_s g_0\theta\left(\frac{4}{d_p}\sqrt{\frac{\theta}{\pi}}\right) \quad (8)$$

(d) Radial distribution function (g_0);

$$g_0=\left[1-\left(\frac{\varepsilon_s}{\varepsilon_{s,max}}\right)^{1/3}\right]^{-1} \quad (9)$$

(e) Solid particle phase pressure (P_s);

$$P_s=\varepsilon_s\rho_s\theta[1+2g_0\varepsilon_s(1+e)] \quad (10)$$

(f) Solid particle phase shear viscosity (μ_s);

$$\mu_s=\frac{4}{5}\varepsilon_s\rho_s d_p g_0(1+e)\sqrt{\frac{\theta}{\pi}}+\frac{10\rho_s d_p\sqrt{\pi\theta}}{96(1+e)g_0\varepsilon_s}\left[1+\frac{4}{5}g_0\varepsilon_s(1+e)\right]^2 \quad (11)$$

(g) Solid particle phase bulk viscosity (ξ_s);

$$\xi_s=\frac{4}{3}\varepsilon_s\rho_s d_p g_0(1+e)\sqrt{\frac{\theta}{\pi}} \quad (12)$$

(h) Conductivity of the solid particle fluctuating energy (κ_s);

$$\kappa_s=\frac{150\rho_s d_p\sqrt{\theta\pi}}{384(1+e)g_0}\left[1+\frac{6}{5}\varepsilon_s g_0(1+e)\right]^2+2\rho_s\varepsilon_s^2 d_p(1+e)g_0\sqrt{\frac{\theta}{\pi}} \quad (13)$$

(i) Exchange of the solid particle fluctuating energy between phases (φ_{gs});

$$\varphi_{gs}=-3\beta_{gs}\theta \quad (14)$$

Table 2. Continued

(j) Gas-solid particle phase interphase exchange coefficient (β_{gs});

- Gidaspow model;

when $\varepsilon_g > 0.80$;

$$\beta_{gs} = 150\frac{(1-\varepsilon_g)^2\mu_g}{\varepsilon_g d_p^2} + 1.75\frac{(1-\varepsilon_g)\rho_g|v_g - v_s|}{d_p} \quad (15)$$

when $\varepsilon_g \leq 0.80$;

$$\beta_{gs} = \frac{3}{4}\frac{(1-\varepsilon_g)\varepsilon_g}{d_p}\rho_g|v_g - v_s|C_{D0}\varepsilon_g^{-2.65} \quad (16)$$

with

$Re < 1000$; $C_{D0} = \frac{24}{Re_k}(1 + 0.15Re_k^{0.687})$; $Re_k = \frac{\rho_g\varepsilon_g|v_g - v_s|d_p}{\mu_g}$

$Re \geq 1000$; $C_{D0} = 0.44$

cles have their own sets of conservation equations. The conservation equations were closed by providing constitutive equations based on the kinetic theory of granular flow, as reviewed by Gidaspow [4]. The conservation and constitutive equations are summarized in Table 2. According to the literature, there was extensive information given on the conservation and constitutive models and the universal values of modeling parameters [17,36,42-44]. Therefore, reasonable models and values from those in the existing literature were selected to use in this study as shown in Tables 1 and 2. About the model validation with the experimental results, it was successfully shown in our previous study [41].

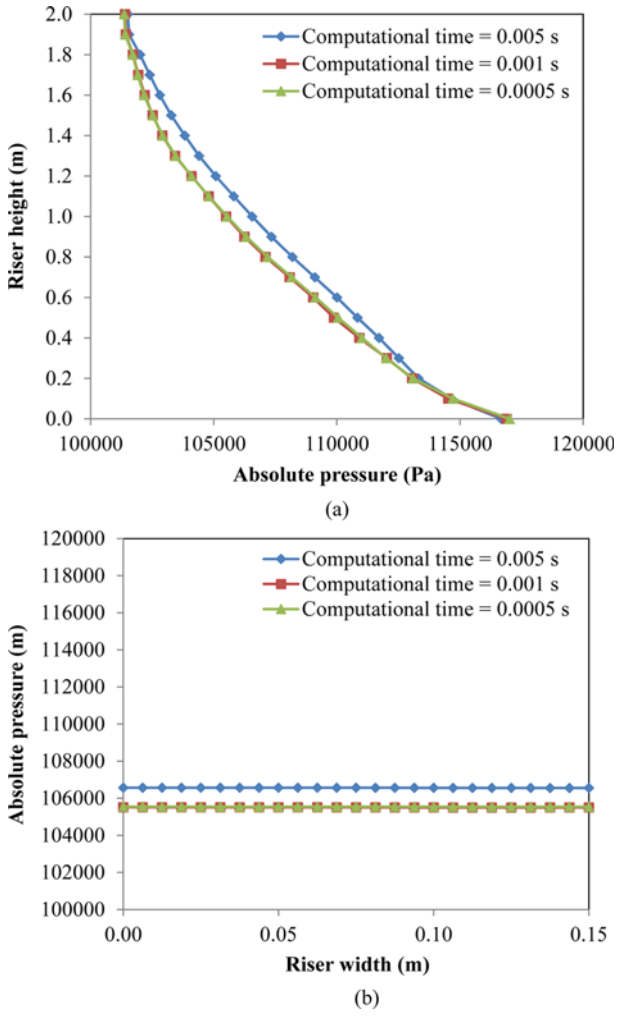

Fig. 3. (a) The axial distributions of time-averaged absolute pressure, and (b) the lateral distributions of time-averaged absolute pressure at 1.00 m CFB riser height with three different computational times.

About the time independence study, the 1.00×10^{-3} s step time with one-hundred iterations per time step was used to ensure numerical stability. The results with various computational times were compared. The largest computational time which does not change the obtained results should be selected to use. In this study, three computational times were varied among 0.005, 0.001 and 0.0005 s with constant 1.25 m/s gas inlet velocity. Fig. 3(a) shows the axial distributions of time-averaged absolute pressure with three different computational times. The lateral distributions of time-averaged absolute pressure with the same three different computational times at 1.00 m CFB riser height are illustrated in Fig. 3(b). At all CFB riser heights, the results with 0.005 s computational time were different from the ones with 0.001 and 0.0005 s computational times. Because this study system of equations is very stiff, the large computational time then gives high erroneous solution or divergence calculation. In the simulation, the quasi-steady state condition was also explored. In this study, four time-averaged ranges were varied, which were 0-10, 10-20, 20-30 and 30-40 s inside the system with gas inlet velocity of 1.25 m/s. The axial distributions of time-averaged absolute pressure with four different time-averaged ranges are displayed in Fig. 4(a). Fig. 4(b) shows the lateral distributions of time-averaged absolute pressure with the same four different time-averaged ranges at 1.00 m CFB riser height. The result with 0-10 s time-averaged range was lower than the results with other time-averaged ranges. Generally, with increasing of system time, the quasi steady state system is obtained. In addition, the fluidization system is the co-current system which feeds from the system bottom. The system variables are then continually stable from the bottom to the top sections. Therefore, the time-averaged distributions of flow variables were computed after the system reached the quasi-steady state conditions, which were the time (t) from 20 s to 40 s. The models were solved by using a computer with Pentium 1.80 GHz CPU 2 GB RAM.

3. Initial and Boundary Conditions

The definition of the appropriate initial and boundary conditions is critical for carrying out a realistic simulation. Initially, the solid particles were filled inside the CFB reactor with a similar value ac-

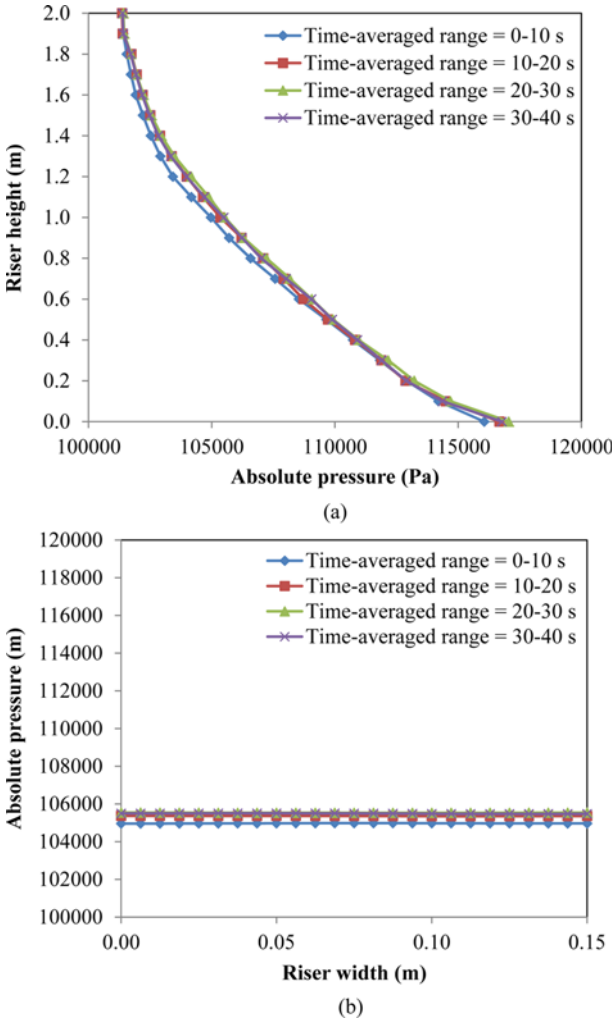

Fig. 4. (a) The axial distributions of time-averaged absolute pressure, and (b) the lateral distributions of time-averaged absolute pressure at 1.00 m CFB riser height with four different time-averaged ranges.

cording to the experimental quantity. The gas inlet velocity was specified at the inlet. In this study, various uniform gas inlet velocities were applied from 0.25 to 25.00 m/s. At the outlet, the system pressure was defined as an atmospheric pressure. The solid particle velocities were set as zero near the system outlet to match with the realistic wire mesh or separating equipment phenomenon. At the wall, a no-slip condition was applied for all velocities, except for the tangential velocity ($v_{t,W}$) and the granular temperature (θ_W) of the solid particle phase. For these variables, the boundary conditions of Johnson and Jackson [45] were used:

$$v_{t,W} = -\frac{6\mu_s\varepsilon_{s,max}}{\pi\phi\rho_s\varepsilon_s g_0\sqrt{3\theta}}\frac{\partial v_{s,W}}{\partial n} \quad (17)$$

$$\theta_W = -\frac{\kappa_s\theta\partial\theta_W}{\gamma_W\partial n} + \frac{\sqrt{3}\pi\phi\rho_s\varepsilon_s v_{s,slip}^2 g_0\theta^{3/2}}{6\varepsilon_{s,max}\gamma_W} \quad (18)$$

where $\gamma_W = \frac{\sqrt{3}\pi(1-e_W^2)\varepsilon_s\rho_s g_0\theta^{3/2}}{4\varepsilon_{s,max}}$, $v_{s,W}$ is velocity of solid particle phase at the wall, $v_{s,slip}$ is slip velocity of solid particle phase at the wall, ε_s is the solid volume fraction and n is unit vector.

RESULTS AND DISCUSSION

After the CFD simulation model was declared, the system hydrodynamics inside high solid particle density CFB riser was explained. The results with various primary gas inlet velocities were compared. Each selected gas inlet velocity represents each specific system fluidization regimes or flow patterns.

1. Solid Volume Fraction

The instantaneous contours of solid volume fraction inside the CFB reactor at 40 s simulation time with six different gas inlet velocities are depicted in Fig. 5. The red contour color means high solid volume fraction, while the blue contour color means low solid volume fraction. Similar to the conventional low solid particle concentration CFB reactor, the system could be divided into batch and continuous fluidizations. At low gas inlet velocities (0.25 and 0.75 m/s), the reactors were operated in batch fluidization where the solid particles inside the system were only dispersed in the CFB riser. At 0.25 m/s gas inlet velocity, the lowest amount of gas being injected into the reactor, the solid particles broadened and the gas started coalescence as gas bubbles. With this observed system hydrodynamics, the system was operating in bubbling fluidization regime [3]. At 0.75 m/s gas inlet velocity, the system consisted of two zones: dense at the bottom section and dilute at the top section. In the bottom section, vigorous mixing occurred inside the reactor, while in the top section, the gas bubbles broke and pushed the solid particles at the roof of gas bubble out of the bed surface. With this flow regime, the bed surface was unclearly seen. The system was operated in turbulent fluidization regime [2]. At high gas inlet velocities (1.25, 5.00, 10.00 and 25.00 m/s), the reactors were operated in continuous fluidization. With all these operating conditions, the solid particles were elutriated of the CFB riser. At 1.25 m/s gas inlet velocity, the first unconventional flow pattern or fluidization regime was observed inside the high solid particle concentration CFB reactor. The solid particles just reached the top section of the system. The solid particle distribution was dense all along the CFB riser both in the lateral and axial system directions. With this condition, the system was operated in circulating-turbulent fluidization regime. Unlike the other experimental literature [38-40], this circulating-turbulent fluidization regime was proved to occur without the secondary gas injection. This observation confirms the CFD literature study by Chalermsinsuwan et al. [21]. At 5.00 m/s gas inlet velocity, the solid particles were dense and dilute at the wall and center sections, respectively. This flow pattern was commonly observed with so-called core-annulus flow structure [18,46]. The system was operated in fast fluidization regime. In the studies by Issangya et al. [34] and Kim et al. [25], a dense suspension upflow pattern occurred at the bottom section inside fast fluidization regime in the high solid particle density CFB reactor, together with this fast fluidization regime. The phenomenon is only observed in the system with high gas inlet velocity or has enough supporting force. With increasing of gas inlet velocity (10.00 m/s), only a small amount of solid particles was observed inside the CFB riser. The solid particles were homogeneously and dilutely distributed [1]. This flow regime was called the pneumatic transport fluidization regime. At 25.00 m/s gas inlet velocity, another

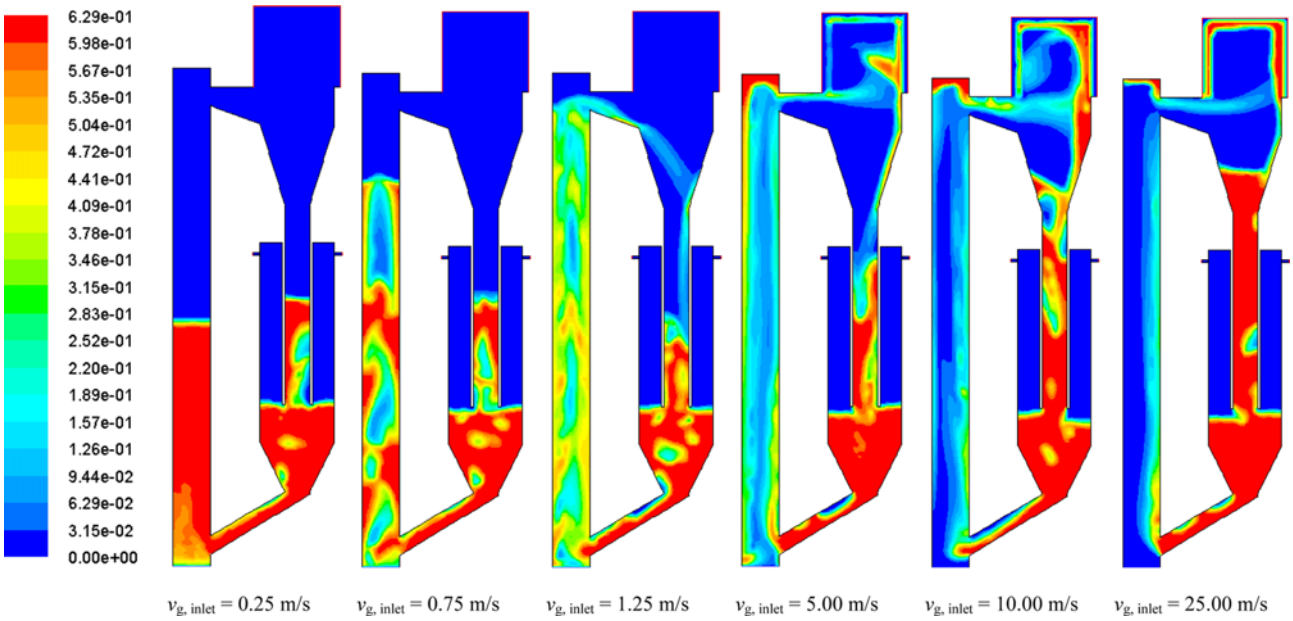

Fig. 5. The instantaneous contours of solid volume fraction inside CFB reactor at 40 s simulation time with six different gas inlet velocities ($v_{g, inlet}$) or fluidization regimes.

unconventional flow pattern or fluidization regime was observed inside the high solid particle concentration CFB reactor. With this gas inlet velocity, the solid particles were dense and dilute at the bottom and top sections, respectively, similar to the turbulent fluidization regime. However, the solid particles were only moved up at one side wall due to the high gas inlet velocity and high solid particle concentration conditions. Because this is the first time finding of this flow regime, the name of this flow regime is not formally assigned. From its flow structure, this flow regime is called "dense suspension bypassing fluidization regime".

Fig. 6 shows the axial distributions of time-averaged solid volume fraction with six different gas inlet velocities or fluidization regimes. For the 0.25 m/s gas inlet velocity or bubbling fluidization regime, the solid particles are only located at the bottom section of CFB riser [3]. This is because of the insufficient force induced by the low gas inlet velocity. For the 0.75 m/s gas inlet velocity or turbulent fluidization regime, the profile confirmed the occurrence of the dense and dilute regions at the bottom and top sections of the CFB riser, respectively. For the 1.25 m/s gas inlet velocity or circulating-turbulent fluidization regime, unconventional system hydrodynamics was observed because of the proper force balancing inside the system. With this flow regime, a uniform solid particle distribution in axial direction was obtained with the solid volume fraction of about 0.30. This unique system characteristic is different from the turbulent and fast fluidization regimes [2,18]. For the 5.00 m/s gas inlet velocity or fast fluidization regime, the commonly s-shaped solid particle profile was observed. This can be explained by the entrance and exit effects [47,48]. For the 10.00 m/s gas inlet velocity or pneumatic transport fluidization regime, the s-shaped solid particle profile was also obtained similar to the fast fluidization regime. However, the solid volume fraction was much lower (approximately 0.10). This profile is similar to the experimental study by Yang [6] and Jaiboon et al. [16]. For the 25.00 m/s gas inlet velocity or dense suspension bypassing fluidization regime, still the axial solid particle distribution was obtained similar to the pneumatic transport fluidization regime with lower solid volume fraction. However, the effect of inlet configuration was ambiguously seen, because of the high gas inlet velocity operating condition.

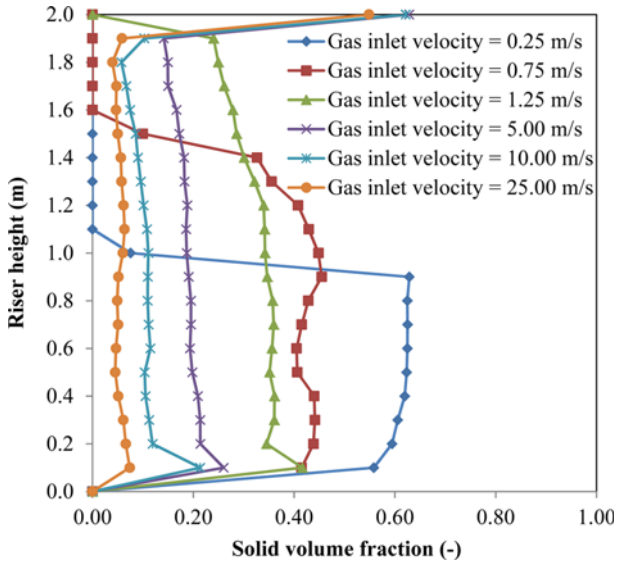

Fig. 6. The axial distributions of time-averaged solid volume fraction with six different gas inlet velocities or fluidization regimes.

The lateral distributions of time-averaged solid volume fraction with six different gas inlet velocities or fluidization regimes at (a) 0.50 m, (b) 1.00 m and (c) 1.50 m CFB riser heights are displayed in Fig. 7. For this figure, the ¼ and ¾ of riser heights were also plotted to better compare the obtained system hydrodynamics. For the 0.25 m/s gas inlet velocity or bubbling fluidization regime, the solid volume fraction was constant over the width of CFB riser at all the riser heights. However, the solid volume fraction was dense only at the

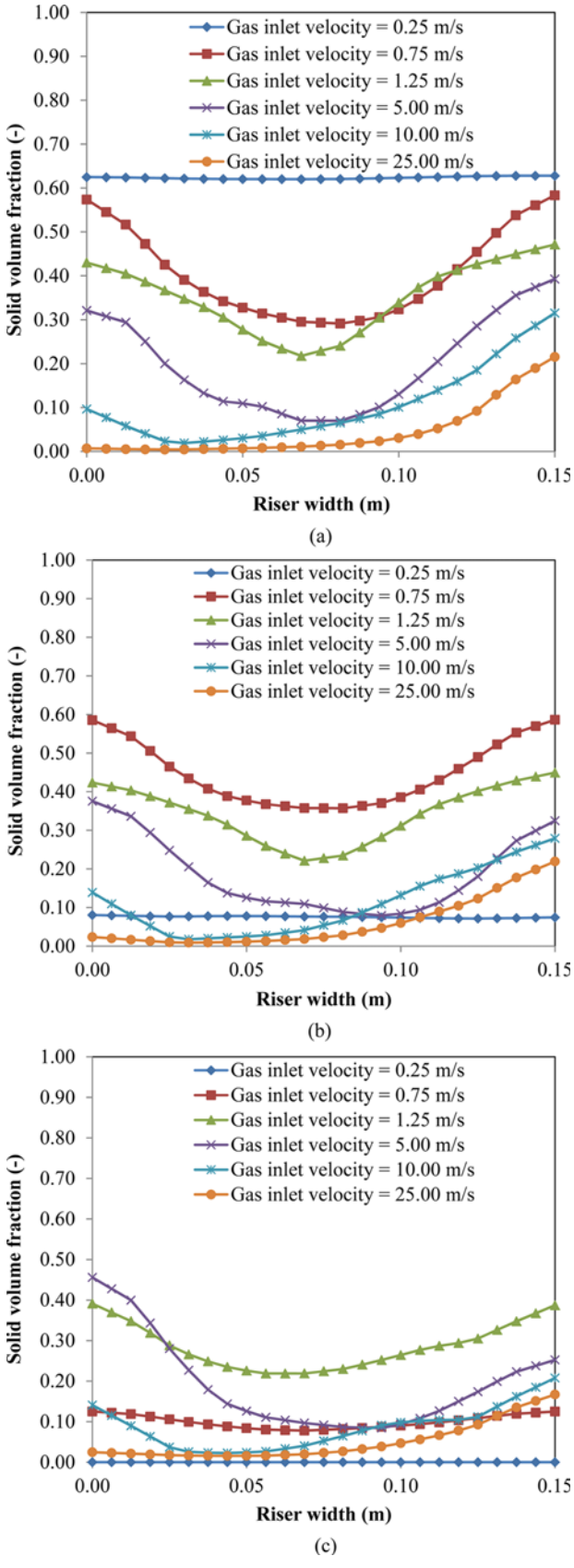

Fig. 7. The lateral distributions of time-averaged solid volume fraction with six different gas inlet velocities or fluidization regimes at (a) 0.50 m, (b) 1.00 m and (c) 1.50 m CFB riser heights.

0.50 m riser height while dilute at the 1.00 and 1.50 m riser heights due to the system hydrodynamics. At higher gas inlet velocities (0.75, 1.25, 5.00 and 10.00 m/s gas inlet velocities), non-uniform solid volume fraction profiles across the riser width are observed in the figure. The solid volume fractions are low and high at the center and wall regions, respectively. For the 0.75 m/s gas inlet velocity or turbulent fluidization regime, the solid volume fractions are lower with the increasing of riser height similar to the bubbling fluidization regime. For the 1.25 m/s gas inlet velocity or circulating-turbulent fluidization regime, uniform solid volume fractions were obtained throughout the CFB riser. This is the distinction of this fluidization regime over the other conventional flow regimes. For the 5.00 m/s gas inlet velocity or fast fluidization regimes, the trends are similar to the ones in circulating-turbulent fluidization regime. However, the general core-annulus flow was more pronounced, especially at the upper CFB riser height [18]. For the 10.00 m/s gas inlet velocity or pneumatic transport fluidization regime, unsymmetrical profiles were obtained at all the CFB riser heights with lower solid volume fraction compared to the previous four flow regimes. For the 25.00

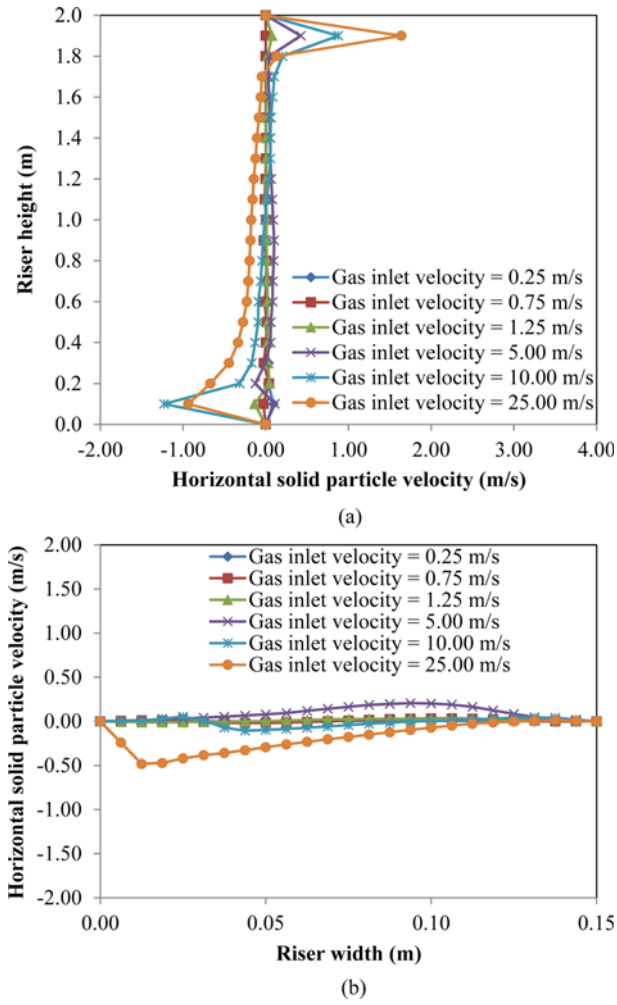

Fig. 8. (a) The axial distributions of time-averaged horizontal solid particle velocity, and (b) the lateral distributions of time-averaged horizontal solid particle velocity at 1.00 m CFB riser height with six different gas inlet velocities or fluidization regimes.

m/s gas inlet velocity or dense suspension bypassing fluidization regime, the solid volume fraction was low and high at two opposite walls of CFB riser. With this asymmetrical flow pattern, the solid particles slid through one CFB riser wall near the solid particle inlet.

2. Solid Particle Velocities

Fig. 8(a) shows the axial distributions of time-averaged horizontal solid particle velocity with six different gas inlet velocities or fluidization regimes. The positive value means most of the solid particles move from the left wall to the right wall, while the negative value means most of the solid particles move in the opposite direction. For all the gas inlet velocities, the horizontal solid particle velocities are high near the top and bottom sections of the CFB riser. This can be explained by the effect of solid particle inlet and outlet channels. At the top of the CFB riser, positive values were obtained, which means that the solid particles are moved out of the system. At the bottom of the CFB riser, negative values are observed, meaning that the solid particles are moved into the system. Along the height of the CFB riser, symmetrical flow patterns are observed, as can be seen by the zero horizontal solid particle velocity values for the 0.25, 0.75 and 1.25 m/s gas inlet velocities. The solid particles are distributed in the opposite direction across the width of the CFB riser. However, unsymmetrical flow patterns are observed with higher gas inlet velocities (for the 5.00, 10.00 and 25.00 m/s gas inlet velocities), as can be seen by the deviation of horizontal solid particle velocity values from zero axis. When comparing among gas inlet velocities, the higher gas inlet velocity gives a higher horizontal solid particle velocity. This situation is consistent with the energy that is put into the system. With increasing CFB riser height, the horizontal solid particle velocities have less amplitude. This can be explained by the energy dissipation of solid particles along the height CFB riser. The lateral distributions of time-averaged horizontal solid particle velocity with six different gas inlet velocities or fluidization regimes at 1.00 m CFB riser height are illustrated in Fig. 8(b). At low gas inlet velocity (for the 0.25, 0.75 and 1.25 m/s gas inlet velocities), most of the solid particles are moved to the system wall. This can be seen by the positive and negative values of horizontal solid velocity at the right and left system wall, respectively. At high gas inlet velocities (for the 5.00, 10.00 and 25.00 m/s gas inlet velocities), unsymmetrical flow patterns are clearly seen. This can be explained by the single positive or negative values throughout the width of CFB riser. As stated above, the higher gas injection velocity, the higher horizontal solid particle velocity was observed.

Fig. 9(a) shows the axial distributions of time-averaged vertical solid particle velocity with six different gas inlet velocities or fluidization regimes. At low gas inlet velocities (for the 0.25, 0.75 and 1.25 m/s gas inlet velocities), the vertical solid particle velocities remain constant throughout the CFB riser. At high gas inlet velocity (for the 5.00, 10.00 and 25.00 m/s gas inlet velocities), the vertical solid particle velocities gradually increase with the increasing of CFB bed riser's height. This is because a system with low gas inlet velocity reaches the quasi steady state condition faster (at shorter CFB riser's height) than the one with high gas inlet velocity. When comparing between gas inlet velocities, the vertical solid particle velocity increases with the increasing of gas inlet velocity. For the 25.00 m/s gas inlet velocity or dense suspension bypassing fluidization regime, the low solid volume fraction inside the CFB riser is accelerated by the high gas inlet velocity. The lateral distributions

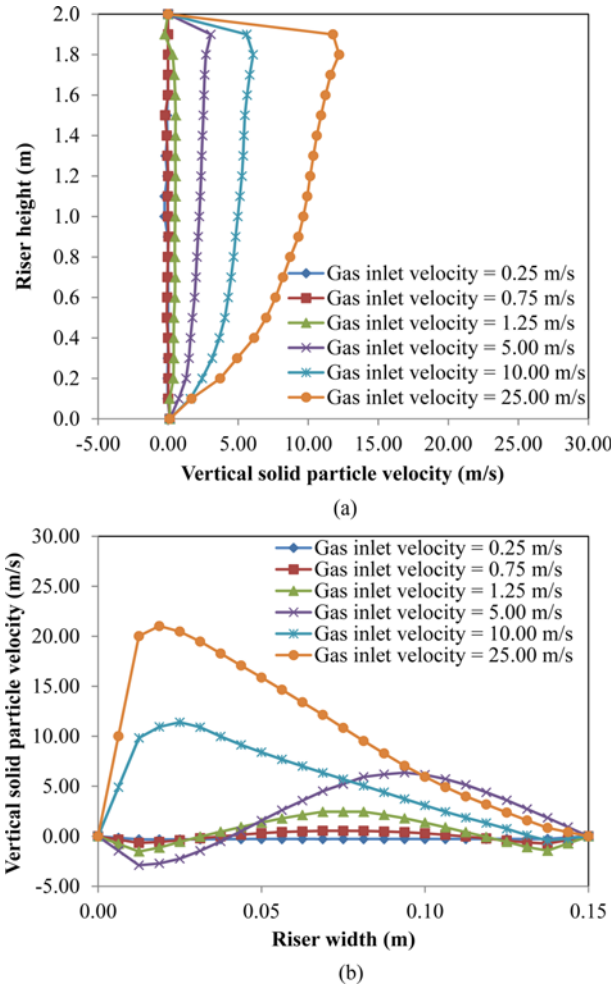

Fig. 9. (a) The axial distributions of time-averaged vertical solid particle velocity, and (b) the lateral distributions of time-averaged vertical solid particle velocity at 1.00 m CFB riser height with six different gas inlet velocities or fluidization regimes.

of time-averaged vertical solid particle velocity with six different gas inlet velocities or fluidization regimes at 1.00 m CFB riser height are shown in Fig. 9(b). The positive and negative values of vertical solid particle velocity mean the upward and downward solid particles, respectively. For the 0.25, 0.75 and 1.25 m/s gas inlet velocities, the symmetrical vertical solid particle velocity profiles over the CFB riser column are observed. The vertical solid particle velocities are high and low near the system center and wall, respectively. However, the vertical solid particle velocity values are not much different due to the low gas inlet velocity. For the 5.00, 10.00 and 25.00 m/s gas inlet velocities, the unsymmetrical vertical solid particle velocity profiles over the CFB riser column were found. For the 5.00 m/s gas inlet velocity or fast fluidization regime, the solid particle was moved up at one side wall and down at the other side wall. This may be because of the selected CFB's height. At some other heights, the high and low vertical solid particle velocities near the system center and wall were also obtained. The observed vertical solid particle velocity flow patterns were still the conventional core-annulus flow pattern [2,18,46]. For the 10.00 and 25.00 m/s

gas inlet velocities, all the solid particles were extremely moved up at one side wall inside the CFB column. At the other side wall, the vertical solid particle velocities were lower due to the circulation of solid particles from the CFB downer. Similar to the results in Fig. 9(a), the vertical solid particle velocities were increased with the increasing of gas inlet velocity.

3. Normal Reynolds Stresses

The normal Reynolds stress represents the production of additional stresses due to random velocity fluctuations, which is characteristic of turbulent flow. It is calculated by the square of the difference between the instantaneous solid particle velocity and time-averaged solid particle velocity. There are the normal Reynolds stresses both in the vertical and horizontal directions. Matonis et al. [49], Jiradilok et al. [50] and Chalerminsuwan et al. [43] used this method for computation of the stresses for two- and three-phase flow systems. The high value implies high additional stresses or fluctuations. Fig. 10(a) illustrates the axial distributions of time-averaged horizontal normal Reynolds stress with six different gas inlet velocities or fluidization regimes. For all the gas inlet velocities except the one with 0.75 m/s gas inlet velocity or turbulent fluidization regime, the horizontal normal Reynolds stresses are high at the top and bottom sections, because of the effect of inlet and outlet configurations. With increasing gas inlet velocity, the higher of the horizontal normal Reynolds stresses were obtained. For the 0.75 m/s gas inlet velocity or turbulent fluidization regime, the horizontal normal Reynolds stress was high and low at the bottom and top sections of the CFB riser, respectively. With this batch fluidization regime, dense solid particles were recirculated at the bottom section of the CFB riser, which produced large additional stresses or turbulences inside this system section. For the 0.25 m/s gas inlet velocity or bubbling fluidization regime, dense solid particles were also observed. However, solid particles have low velocity and are less recirculated. Therefore, less horizontal normal Reynolds stresses was found when compared to the turbulent fluidization regime. The lateral distributions of time-averaged horizontal normal Reynolds stress with six different gas inlet velocities or fluidization regimes at 1.00 m CFB riser height are displayed in Fig. 10(b). The horizontal normal Reynolds stresses increased with the increasing of gas inlet velocity. However, simi-

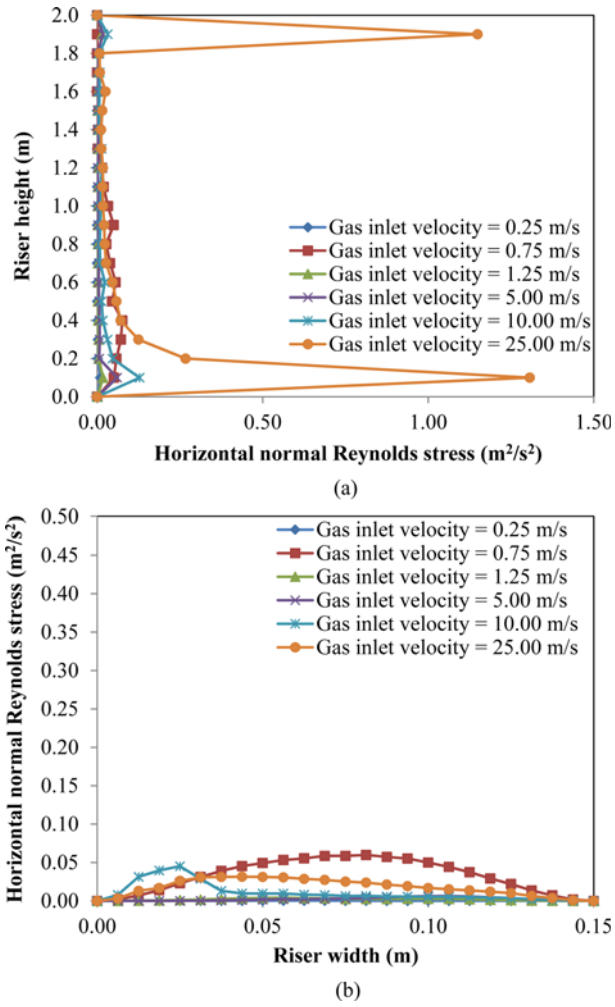

Fig. 10. (a) The axial distributions of time-averaged horizontal normal Reynolds stress, and (b) the lateral distributions of time-averaged horizontal normal Reynolds stress at 1.00 m CFB riser height with six different gas inlet velocities or fluidization regimes.

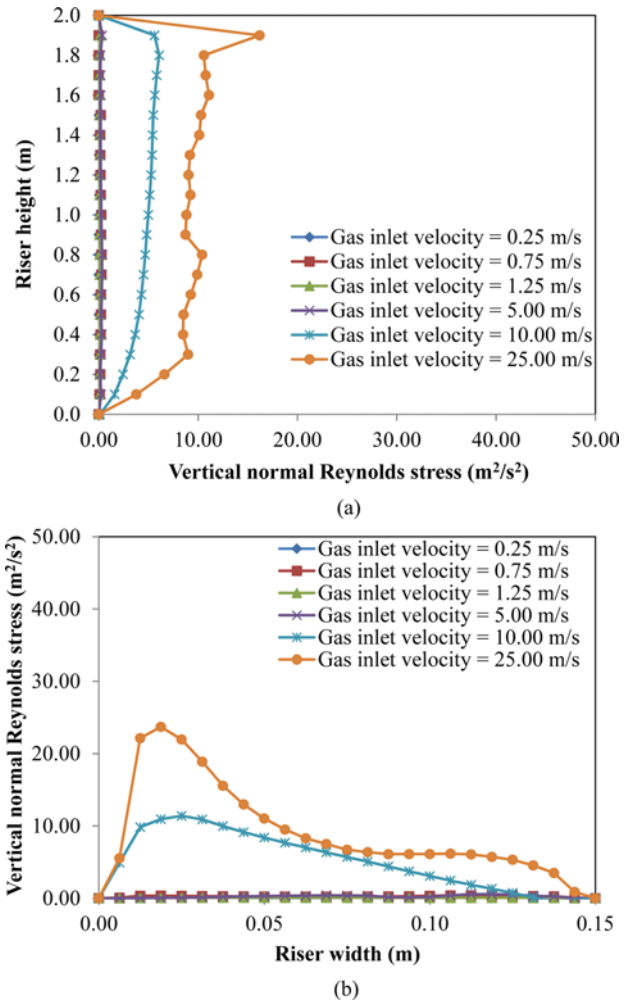

Fig. 11. (a) The axial distributions of time-averaged vertical normal Reynolds stress, and (b) the lateral distributions of time-averaged vertical normal Reynolds stress at 1.00 m CFB riser height with six different gas inlet velocities or fluidization regimes.

lar to the results in Fig. 10(a), the horizontal normal Reynolds stresses had different trend for 0.75 m/s gas inlet velocity or turbulent fluidization regime. In the figure, there are the points that had a horizontal normal Reynolds stress peak near the wall region at opposite direction of solid particle inlet from the CFB downer (especially for 10.00 and 25.00 m/s gas inlet velocities). At this position, high fluctuation of solid particle velocity or significantly changed in solid particle flow pattern was obtained. The solid particles may move in and out from the core and annulus regions of the CFB riser.

Fig. 11(a) shows the axial distributions of time-averaged vertical normal Reynolds stress with six different gas inlet velocities or fluidization regimes. For all the gas inlet velocities, the vertical normal Reynolds stresses were increased with the increasing of gas inlet velocity. The vertical normal Reynolds stresses remained constant throughout the system for the 10.00 and 25.00 m/s gas inlet velocities. This is because the same system hydrodynamics is observed inside these two fluidization regimes. For the low gas inlet velocities (0.25, 0.75, 1.25 and 5.00 m/s gas inlet velocities), the trend of vertical normal Reynolds stresses was not clearly seen due to the x-axis's scale. Though, with the same explanation, constant profiles were predicted for the 1.25 and 5.00 m/s gas inlet velocities due to their fluidization flow pattern. For the 0.25 and 0.75 m/s gas inlet velocities, the expected profiles should be high and low at the bottom and top sections of CFB riser. Comparing between vertical and horizontal system directions, the vertical one had higher values than the horizontal one, because the vertical direction is the main flow direction. The lateral distributions of time-averaged vertical normal Reynolds stress with six different gas inlet velocities or fluidization regimes at 1.00 m CFB riser height are shown in Fig. 11(b). The vertical normal Reynolds stresses increased with the increasing of gas inlet velocity. Similar to the result in the previous figure, the highest vertical normal Reynolds stress was obtained with the 25.00 m/s gas inlet velocity or dense suspension bypassing fluidization regime. The peak of vertical normal Reynolds stress implies high fluctuation in the bypassing zone of the CFB riser. For the same reason, high values of vertical normal Reynolds stress were obtained for the 10.00 m/s gas inlet velocity or pneumatic transport fluidization regime. This is because high turbulence or fluctuation occurred at that system position. In addition, the results confirmed that the vertical normal Reynolds stress had higher values than the horizontal one due to the solid particle trajectory inside the system.

4. Total Granular Temperature

The granular temperature is used to determine the oscillations, both due to solid particles and due to particle clusters [51]. Kashyap et al. [52] showed using a kinetic theory based particle image velocity method that there are two kinds of turbulence in fluidization: a laminar and turbulent. The laminar type is due to random oscillations of individual solid particles, measured by the classical granular temperature. The CFD program itself computes the laminar granular temperature by solving the governing equation. The turbulent type is caused by the motion of clusters of solid particles or bubbles, measured by the average particle normal Reynolds stress, which is the average of the three squares of the velocity components in all the system directions. The sum of the granular temperatures due to the solid particle oscillations and due to the particle cluster oscillations is the total granular temperature. The high value of total granular temperature means high system oscillation. Fig. 12(a) displays

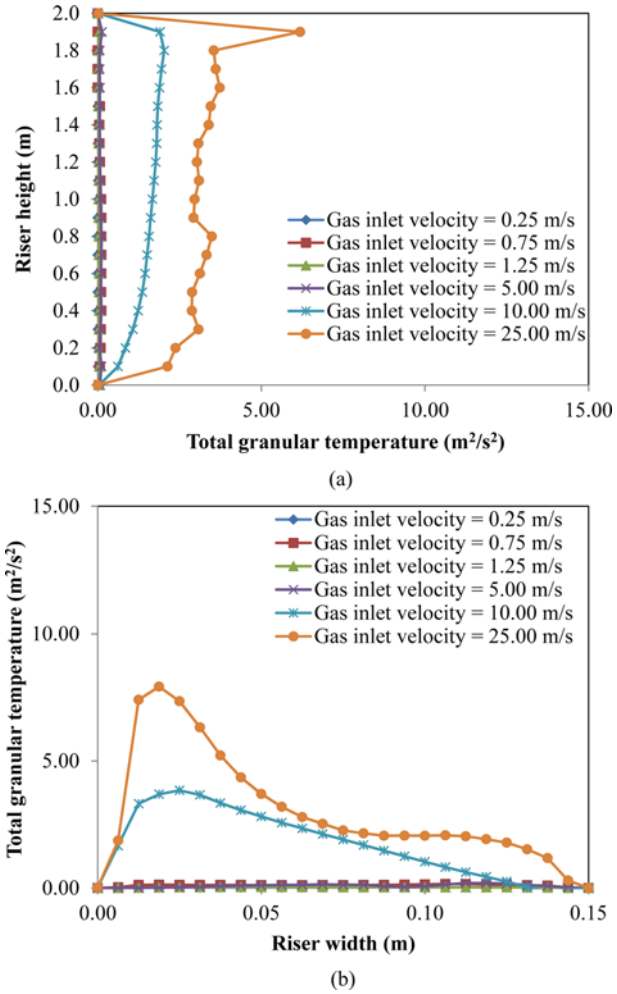

Fig. 12. (a) The axial distributions of time-averaged total granular temperature, and (b) the lateral distributions of time-averaged total granular temperature at 1.00 m CFB riser height with six different gas inlet velocities or fluidization regimes.

the axial distributions of time-averaged total granular temperature with six different gas inlet velocities or fluidization regimes. Similar to the normal Reynolds stresses, the total granular temperature increased with increasing gas inlet velocity due to the high feeding energy. This is clearly seen for the 10.00 and 25.00 m/s gas inlet velocities. For the other low gas inlet velocities, the total granular temperatures were not differentiable because of the employed graphical scale. The effect of gas inlet velocity or fluidization regime will be discussed in detail in the following figures. From all the obtained results, the turbulence was slightly higher at the top section of the CFB riser than at the bottom one. This can be explained by the effect of system outlet configuration. The lateral distributions of time-averaged total granular temperature with six different gas inlet velocities or fluidization regimes at 1.00 m CFB riser height are shown in Fig. 12(b). The total granular temperature with the highest gas inlet velocity had the highest values. Still, the trend was not clearly seen for the low gas inlet velocities (0.25, 0.75, 1.25 and 5.00 m/s gas inlet velocities). The total granular temperature peaks near the wall region at opposite direction of solid particle inlet from the CFB

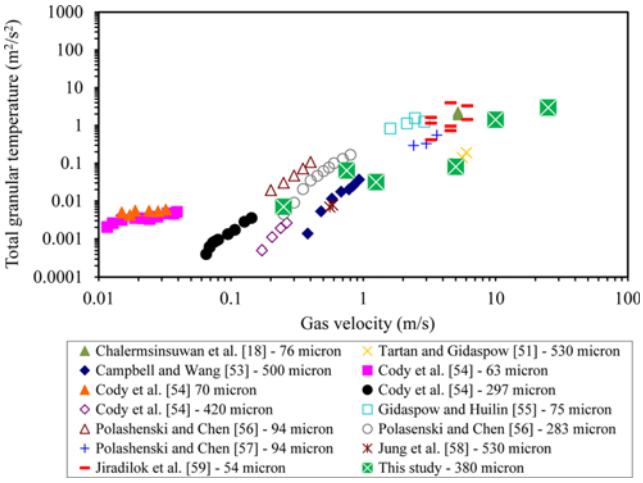

Fig. 13. The effect of gas inlet velocity on total granular temperature compared with different literature values.

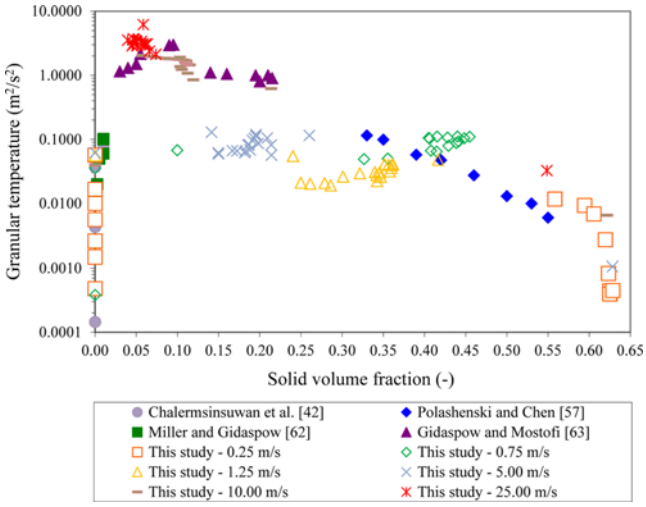

Fig. 14. The effect of solid volume fraction on total granular temperature compared with different literature values.

downer were also observed. This also confirms that high system turbulence or fluctuation is occurring at those system positions.

Fig. 13 illustrates the effect of gas inlet velocity on total granular temperature compared with different literature values. In the figure, various experimental and CFD results are plotted to compare and verify with this study's results [18,51,53-59]. The obtained results are in the range of the literature information with the same gas inlet velocity. For the 0.25 m/s gas inlet velocity or bubbling fluidization regime, the total granular temperature is the lowest compared to the other fluidization flow regimes. This is because the lowest gas inlet velocity was employed. For the 0.75 m/s gas inlet velocity or turbulent fluidization regime, the total granular temperature is higher when compared to the one with the 0.25 m/s gas inlet velocity or bubbling fluidization regime. For the 1.25 m/s gas inlet velocity or circulating turbulent fluidization regime, the total granular temperature is lower than the one with the 0.75 m/s gas inlet velocity or turbulent fluidization regime. The system hydrodynamics expresses this phenomenon. This implies that the oscillation inside this unconventional fluidization regime is low. The dense solid particles will reside in the system with longer residence time. This operating condition will be the suitable choice for the sorption application [21,60]. As the gas inlet velocity was increased to 5.00, 10.00 and 25.00 m/s, the total granular temperatures were then linearly increased. The higher of gas inlet velocity induces the higher system oscillation or total granular temperature. For the 25.00 m/s gas inlet velocity or dense suspension bypassing fluidization regime, the highest total granular temperature was obtained. The solid particles will reside in the system with shortest residence time. This operating condition will be the appropriate option for the solid particle transportation application [61].

Another comparison of total granular temperature with the literature information is shown in Fig. 14. The effect of solid volume fraction on total granular temperature compared with different literature values is displayed [42,57,62,63]. There is a maximum point of total granular temperature with different values of solid volume fraction. With low solid volume fraction, there are no solid particles in the system. Therefore, the oscillation is low. With high solid volume fraction, the solid particles are packed together. The oscillation is then also low. For the 0.25 m/s gas inlet velocity or bubbling fluidization regime, the total granular temperature has two zones according to the system hydrodynamics: the bottom dense and top dilute. The values are consistent with the total granular temperature values in the literature. For the 0.75 m/s gas inlet velocity or turbulent fluidization regime, the total granular temperatures in the bottom region are consistent with the range in the literature. However, the total granular temperatures in the top region are slightly lower than the literature values. This is because of the difference between dense solid particle flux in this study and dilute solid particle flux in the literature. For the 1.25 and 5.00 m/s gas inlet velocities or circulating-turbulent fluidization and fast fluidization regimes, the total granular temperatures are lower than the expected literature values. Similar to the turbulent fluidization regime, the dense solid particle flux is the main reason for these predicted low values. This figure also confirms the low values of total granular temperature for circulating-turbulent fluidization regime across the system. For the 10.00 m/s gas inlet velocity or pneumatic transport fluidization regime, the values are in the same range as the literature values. For the 25.00 m/s gas inlet velocity or dense suspension bypassing fluidization regime, the highest values of total granular temperature are observed. Still, the values are consistent with the literature values.

CONCLUSIONS

We investigated the system hydrodynamics inside a high solid particle concentration CFB reactor using commercial CFD simulation program called ANSYS FLUENT. From the results, the conventional fluidization regimes were observed inside the system, including bubbling, turbulent, fast fluidization and pneumatic transport regimes. In addition, two unconventional fluidization regimes were observed with only primary gas injection feeding. The circulating-turbulent fluidization regime showed uniformly dense solid particle distribution in both the axial and lateral system directions, while the dense suspension bypassing fluidization regime exhibited solid particle flow at only one side system wall. Then, the comprehensively fluidization regime clarification and mapping were eval-

uated using in-depth system parameters, which were normal Reynolds stresses and total granular temperature. From all the obtained results, the total granular temperature values had the same trend with the normal Reynolds stresses. For the circulating-turbulent fluidization regime, the total granular temperature was minimum compared to the adjacent fluidization regimes due to its flow pattern. The highest total granular temperature was observed inside the dense suspension bypassing fluidization regime. There was a maximum point of total granular temperature with different values of solid volume fraction. With low solid volume fraction, there is no solid particle in the system. Thus, the oscillation is low. With high solid volume fraction, the solid particles are packing together. This also makes the oscillation to be low. The circulating-turbulent fluidization and dense suspension bypassing fluidization regimes will be the suitable choices for the sorption and solid particle transportation applications, respectively.

ACKNOWLEDGEMENTS

This study was financially supported by grants from the Thailand Research Fund and the Commission on the Higher Education for fiscal year 2012-2014 (MRG5580140), the grant for Development of New Faculty Staff (Ratchadaphisek Somphot Endowment Fund) of Chulalongkorn University, the grant from Faculty of Science of Chulalongkorn University and the Center of Excellence on Petrochemical and Materials Technology, Chulalongkorn University.

REFERENCES

1. J. R. Grace, A. A. Avidan and T. M. Knowlton, *Circulating fluidized beds*, Blackie Academic and Professional, London (1997).
2. P. Basu, *Combustion and gasification in fluidized beds*, CRC Press, New York (2006).
3. D. Kunii and O. Levenspiel, *Fluidization engineering*, Butterworth-Heinemann, Boston (1991).
4. D. Gidaspow, *Multiphase flow and fluidization: Continuum and kinetic theory description*, Academic Press, Boston (1994).
5. M. Rhodes, *Introduction to particle technology*, Wiley, West Sussex, UK (2008).
6. W. C. Yang, *Handbook of fluidization and fluid-particle systems*, Marcel Dekker, Inc., New York (2003).
7. H. Masuda, K. Higashitani and H. Yoshida, *Powder technology: Handling and operations, process instrumentation, and working hazards*, CRC Press, Boca Raton, FL (2006).
8. B. Chalermsinsuwan, P. Kuchonthara and P. Piumsomboon, *Chem. Eng. Process.*, **49**, 1144 (2010).
9. D. Gidaspow and V. Jiradilok, *Computational techniques: The multiphase CFD approach to fluidization and green energy technologies*, Nova Science Publishers, Inc., New York (2010).
10. H. T. Bi and J. R. Grace, *Int. J. Multiphase Flow*, **21**(6), 1229 (1995).
11. B. Chalermsinsuwan and P. Piumsomboon, *Chem. Eng. Sci.*, **66**, 5602 (2011).
12. E. Rabinovich and H. Kalman, *Powder Technol.*, **207**(1-3), 119 (2011).
13. X. Gao, C. Wu, Y. W. Cheng, L. J. Wang and X. Li, *Powder Technol.*, **228**, 1 (2012).
14. Y. T. Makkawi and P. C. Wright, *Chem. Eng. Sci.*, **57**(13), 2411 (2002).
15. Q. F. Hou, Z. Y. Zhou and A. B. Yu, *Chem. Eng. Sci.*, **84**, 449 (2012).
16. O. Jaiboon, B. Chalermsinsuwan, L. Mekasut and P. Piumsomboon, *Powder Technol.*, **233**, 215 (2013).
17. A. Almuttahar and F. Taghipour, *Powder Technol.*, **185**(1), 11 (2008).
18. B. Chalermsinsuwan, P. Piumsomboon and D. Gidaspow, *Chem. Eng. Sci.*, **64**, 1195 (2009).
19. G. Guan, C. Fushimi, A. Tsutsumi, M. Ishizuka, S. Matsuda, H. Hatano and Y. Suzuki, *Particuology*, **8**(6), 602 (2010).
20. M. Qi, S. Barghi and J. Zhu, *Chem. Eng. J.*, **209**, 633 (2012).
21. B. Chalermsinsuwan, P. Piumsomboon and D. Gidaspow, *AIChE J.*, **56**, 2805 (2010).
22. Y. Tatemoto, S. Yano, Y. Mawatari, K. Noda and N. Komatsu, *Chem. Eng. Sci.*, **62**(1-2), 471 (2007).
23. F. R. G. B. da Silva, M. de Souza, A. M. de Souza da Costa, L. M. de Matos Jorge and P. R. Paraíso, *Powder Technol.*, **229**, 61 (2012).
24. J. R. Grace, *Powder Technol.*, **113**, 242 (2000).
25. S. W. Kim, G. Kirbas, H. Bi, C. J. Lim and J. R. Grace, *Chem. Eng. Sci.*, **59**, 3955 (2004).
26. Z. Q. Li, C. N. Wu, F. Wei and Y. Jin, *Powder Technol.*, **139**, 214 (2004).
27. J. C. S. C. Bastos, L. M. Rosa, M. Mori, F. Marini and W. P. Martignoni, *Catal. Today*, **130**, 462 (2008).
28. J. Zhu, *Particuology*, **8**, 640 (2010).
29. H. K. Versteeg and W. Malalasekera, *An introduction to computational fluid dynamics: The finite volume method*, Prentice Hall, New Jersey (2007).
30. Fluent, Inc., *Fluent 6.3 User's Guide*, Fluent, Inc., Lebanon (2006).
31. S. Chapman and T. G. Cowling, *The mathematical theory of non-uniform gases*, Cambridge University Press, New York (1970).
32. N. Zhang, B. Lu, W. Wang and J. Li, *Chem. Eng. J.*, **162**(2), 821 (2010).
33. H. Bi and J. Zhu, *AIChE J.*, **39**(8), 1272 (1993).
34. A. S. Issangya, D. Bai, H. T. Bi, K. S. Lim, J. Zhu and J. R. Grace, *Chem. Eng. Sci.*, **54**, 5451 (1999).
35. E. Cruz, F. R. Steward and T. Pugsley, *Powder Technol.*, **169**(3), 115 (2006).
36. A. Almuttahar and F. Taghipour, *Chem. Eng. Sci.*, **63**(6), 1696 (2008).
37. X. Wang, F. Jiang, J. Lei, J. Wang, S. Wang, X. Xu and Y. Xiao, *Appl. Therm. Eng.*, **31**(14-15), 2254 (2011).
38. H. Zhu and J. Zhu, *Chem. Eng. Sci.*, **63**(11), 2920 (2008).
39. M. Qi, J. Zhu and S. Barghi, *Chem. Eng. Sci.*, **84**, 437 (2012).
40. X. Zhu, C. Yang, C. Li, Y. Liu, L. Wang, T. Li and Q. Geng, *Chem. Eng. J.*, **215-216**, 188 (2013).
41. T. Thummakul, P. Piumsomboon and B. Chalermsinsuwan, *CFD simulation of carbon dioxide reduction from flue gas using solid sorbent in circulating fluidized bed reactor*, Master's Degree Thesis, Chulalongkorn University, Bangkok (2013).
42. B. Chalermsinsuwan, D. Gidaspow and P. Piumsomboon, *Chem. Eng. J.*, **171**, 301 (2011).
43. B. Chalermsinsuwan, T. Chanchuey, W. Buakhao, D. Gidaspow and P. Piumsomboon, *Chem. Eng. J.*, **189-190**, 313 (2012).
44. A. Nikolopoulos, N. Nikolopoulos, A. Charitos, P. Grammelis, E. Kakaras, A. R. Bidwe and G. Varela, *Chem. Eng. Sci.*, **90**, 137 (2013).
45. P. C. Johnson and R. Jackson, *J. Fluid Mech.*, **176**, 67 (1987).
46. J. Wang, W. Ge and J. Li, *Chem. Eng. Sci.*, **63**(6), 1553 (2008).
47. M. J. Rhodes, M. Sollaart and X. S. Wang, *Powder Technol.*, **99**(2),

194 (1998).
48. E. R. Monazam, L. J. Shadle, J. S. Mei and J. Spenik, *Powder Technol.*, **155**(1), 17 (2005).
49. D. Matonis, D. Gidaspow and M. Bahary, *AIChE J.*, **48**, 1413 (2002).
50. V. Jiradilok, D. Gidaspow and R. W. Breault, *Chem. Eng. Sci.*, **62**, 3397 (2007).
51. M. Tartan and D. Gidaspow, *AIChE J.*, **50**, 1760 (2004).
52. M. Kashyap, B. Chalermsinsuwan and D. Gidaspow, *Particuology*, **9**(6), 572 (2011).
53. C. Campbell and D. Wang, *J. Fluid Mech.*, **227**, 495 (1991).
54. G. Cody, D. Goldfarb, G. Storch and A, Norris, *Powder Technol.*, **87**, 211 (1996).
55. D. Gidaspow and L. Huilin, *AIChE J.*, **42**, 2503 (1996).
56. W. Polashenski and J. Chen, *Powder Technol.*, **90**, 13 (1997).
57. W. Polashenski and J. Chen, *Ind. Eng. Chem. Res.*, **38**, 705 (1999).
58. J. Jung, D. Gidaspow and I. K. Gamwo, *Ind. Eng. Chem. Res.*, **44**, 1329 (2005).
59. V. Jiradilok, D. Gidaspow, S. Damronglerd, W. J. Koves and R. Mostofi, *Chem. Eng. Sci.*, **61**, 5544 (2006).
60. O. Jaiboon, B. Chalermsinsuwan, L. Mekasut and P. Piumsomboon, *Chem. Eng. J.*, **219**, 262 (2013).
61. K. Svoboda, S. Kalisz, F. Miccio, K. Wieczorek and M. Pohořelý, *Powder Technol.*, **192**(1), 65 (2009).
62. A. Miller and D. Gidaspow, *AIChE J.*, **38**, 1801 (1992).
63. D. Gidaspow and R. Mostofi, *AIChE J.*, **49**, 831 (2003).